Cellular contractile forces emerge from time and F-actin dependent non-mechanosensitive displacements

Lea Feld[1], Lior Kellerman[1], Abhishek Mukherjee[1], Ariel Livne[2],
Eran Bouchbinder[3,*], Haguy Wolfenson[1,*]

[1]Department of Genetics and Developmental Biology, Rappaport Faculty of Medicine, Technion — Israel Institute of Technology, Haifa 31096, Israel

[2]Department of Molecular Cell Biology, Weizmann Institute of Science, Rehovot 7610001, Israel

[3]Department of Chemical and Biological Physics, Weizmann Institute of Science, Rehovot 7610001, Israel

*Correspondance: eran.bouchbinder@weizmann.ac.il; haguyw@technion.ac.il

Abstract

The ability to actively apply contractile forces to their environment and to sense its mechanical properties are fundamental features of cells. The widespread view is that contractile forces are mechanosensitive, i.e. that cells regulate these forces through sensing the rigidity of the environment. Here we use theory and extensive experiments to study the time evolution of cellular contractile forces. We show that they are generated by an intrinsic, time-dependent contractile displacement that is independent of the environment's rigidity. Consequently, whereas contractile forces indeed depend on the environment's rigidity and in fact linearly scale with it, they do so through a purely mechanistic linear force-rigidity relation, i.e. in a non-mechanosensitive manner. Furthermore, we show that the force-generating contractile displacement is directly related to the evolution of the actomyosin network, most notably to the time-dependent concentration of F-actin. The emerging picture of force generation and mechanosensitivity unifies various existing observations on cellular contractility.

Introduction

The mechanical properties of the extracellular matrix (ECM) play critical roles in the most fundamental cellular processes[1]. Matrix rigidity, for instance, affects cell polarization, migration, growth, death, and differentiation[2-9]. Probing ECM mechanical properties ('mechanosensing') and feeding the outcome back into cells ('mechanotransduction') are processes that occur via integrin-based cell-matrix adhesions. These multi-molecular complexes bind the ECM at the extracellular side and attach (indirectly) to the actomyosin cytoskeleton at the intracellular side (see Fig. 1A). The cytoskeleton is composed of a network of actin filaments (F-actin) and myosin motors, where the latter actively generate contractile forces. It is well established that the larger the ECM rigidity is, the larger cellular contractile forces are[10-13]. This correlation is commonly interpreted to be mechanosensitive, i.e. contractile force generation processes are thought to be regulated through feedback from the cell's probing/sensing of the rigidity. It is also well established that cells interacting with more rigid ECMs feature stronger and larger adhesions (classically referred to as 'focal adhesions'), which are accompanied by the formation and growth of thick actin stress fibers that are attached to them[4]. Collectively, these processes have dramatic effects on cellular properties and functions. However, although actomyosin-based cellular contractility is regarded as a fundamental mechanosensing mechanism, a comprehensive understanding of both the contractile force generation process and mechanosensitivity is currently missing.

Here, we address the basic nature and time evolution of cellular contractile forces through a simple mathematical model combined with extensive experiments using cells adhering to micro-pillar arrays[14]. We show that for a broad range of physiologically relevant ECM rigidities, the contractile force is proportional to the ECM rigidity – a result of simple mechanics. The proportionality factor is an intrinsic, cell-specific time-dependent contractile displacement that is *rigidity-independent*. Namely, we demonstrate that cellular contractile forces are themselves generically *non-mechanosensitive*. This fundamental observation implies that information about ECM rigidity is internally and simply encoded at each point in time in the magnitude of the contractile force. We further show that the time-dependent contractile displacement is determined by the time evolution of the F-actin concentration, indicating that the dynamics of myosin motors are not the rate-limiting factor in the cellular force generation process. The emerging picture of active cellular contractility is shown to explain and unify various existing observations.

Results

A simple model of active cellular contractility

The major component of the cellular contractile force machinery is actomyosin networks, which are made up of force transmitting actin structures and force generating myosin motors (Fig. 1A). For adherent cells, the generated contractile force is transferred across the plasma membrane to the ECM through integrins (Fig. 1A). To model how contractile forces are generated, we first assume that the myosin motors intrinsically generate a *time-dependent contractile displacement*, $\Delta(t, k_{ECM})$, which they impose at time t on the actin structures to which they attach and which may depend on the effective rigidity of the ECM, k_{ECM}. Whether or not the contractile displacement depends on k_{ECM} is a major question to be addressed below. Note that the existence of a contractile displacement is in line with the fundamental property of myosin motors, which display a typical working stroke size (namely, distance)[15]. $\Delta(t, k_{ECM})$ is accommodated by the displacement $\delta_{Act}(t)$ of the actin structure and by the deformation $\delta_{ECM}(t)$ of the ECM [16], i.e. $\Delta(t) = \delta_{Act}(t) + \delta_{ECM}(t)$.

The contractile force $F(t, k_{ECM})$ satisfies the coarse-grained force balance equation $F(t, k_{ECM}) = k_{Act}\,\delta_{Act}(t) = k_{ECM}\,\delta_{ECM}(t)$, where k_{Act} is the effective rigidity of the actin structures (Fig. 1B, top panel; see also Supplementary Note 1 & Schwarz et al.[16]), which in turn implies that $F(t, k_{ECM}) = (k_{Act}^{-1} + k_{ECM}^{-1})^{-1}\Delta(t, k_{ECM})$ (see also Supplementary Note 2). In order to proceed, we further assume that for a broad range of physiologically relevant conditions (namely, relatively soft environments), the effective rigidity of actin structures is significantly larger than the rigidity of the ECM, i.e. $k_{Act} \gg k_{ECM}$. With this assumption, to be extensively tested below, we obtain

$$F(t, k_{ECM}) \approx k_{ECM}\,\Delta(t, k_{ECM}) \quad . \tag{1}$$

This equation shows that the dependence of the contractile force on the external rigidity may have two qualitatively different origins. First, the possible mechanosensitive contribution – if it exists – is contained within the contractile displacement $\Delta(t, k_{ECM})$. Second, and independently of the possible k_{ECM}-dependence of $\Delta(t, k_{ECM})$, there exists also a non-mechanosensitive contribution – the overall pre-factor k_{ECM}, which emerges from a linear force-displacement relation of the ECM. Consequently, Eq. (1) demonstrates that the mere existence of a dependence of $F(t, k_{ECM})$ on the external rigidity k_{ECM} does not immediately indicate that the contractile force is mechanosensitive. In fact. Eq. (1) offers a clean procedure

to extract the possible mechanosensitive part of the contractile force by plotting the force $F(t, k_{ECM})$ normalized by k_{ECM}, $F(t, k_{ECM})/k_{ECM}$, a procedure that is followed in our experiments described below.

Note that $F(t, k_{ECM})/k_{ECM}$ simply equals $\delta_{ECM}(t)$, which implies that in the regime $k_{Act} \gg k_{ECM}$, the model predicts also $\delta_{ECM}(t) \approx \Delta(t, k_{ECM})$ and $\delta_{Act}(t) \approx 0$ (see Fig. 1B, middle panel). That is, in this case, the actin filaments/structures are predicted to experience no internal deformation, but rather to slide one relative to another as rigid objects (as they polymerize/de-polymerize at their edges), and the ECM deformation $\delta_{ECM}(t)$ allows direct access to the myosin-generated collective contractile displacement $\Delta(t, k_{ECM})$. Finally, note that in the opposite regime, $k_{Act} \ll k_{ECM}$, relevant to cells adhering to glass/plastic plates, the model predicts $\delta_{Act}(t) \approx \Delta(t, k_{ECM})$ and $\delta_{ECM}(t) \approx 0$ (see Fig. 1B, bottom panel and Supplementary Note 2).

Direct experimental tests

To test whether $\Delta(t, k_{ECM})$ in Eq. (1) depends on k_{ECM}, i.e. whether it is mechanosensitive, we performed extensive experiments on cells adhering to arrays of fibronectin-coated PDMS micro-pillars of 2μm diameter (see Methods and Fig. 2A). We monitored the cells from the very initial stages of attachment to the pillars, and as they were spreading, we tracked the cell-driven pillar deflections, which is simply $\delta_{ECM}(t)$ (Fig. 2A). We used pillars with rigidities that vary by more than 15-fold, $k_{ECM} = 2, 6, 31$ pN/nm, equivalent to effective elastic moduli in the range $E_{eff} \approx 1.5 - 22$ kPa (see Methods), thus allowing us to test the relevance of the relation $k_{Act} \gg k_{ECM}$ to a broad range of physiological conditions[17]. The validity of this relation will not be assessed directly as there are significant uncertainties about the typical value of k_{Act}; instead, we will indirectly assess it through the relation $\delta_{ECM}(t) \approx F(t, k_{ECM})/k_{ECM}$.

To test the generality of our model, we used five cell lines that displayed distinct phenotypic behaviors when adhering to soft and rigid matrices (Supplementary Fig. 1): mouse embryonic fibroblasts (WT-MEFs), MEFs stably expressing paxillin-GFP (pax-GFP), MEFs with stable knockdown of α-actinin (α-act KD), rat embryonic fibroblasts (REF52), and the human breast adenocarcinoma cell line MDA-MB231. For all cell lines, we measured $\delta_{ECM}(t)$ for multiple pillars from the initial rise of pillar displacement until the release (Supplementary Fig. 2), averaged them, and superimposed the results for the widely different rigidities. The outcome, presented in Fig. 2B, is remarkable: for each cell line, $\delta_{ECM}(t)$ collapses on a master curve that is *independent* of the rigidity, despite the more than 15-fold variation in the latter. This result, which indicates that the contractile force $F(t, k_{ECM}) \approx k_{ECM}\,\Delta(t) \approx$

114 $k_{ECM}\,\delta_{ECM}(t)$ trivially depends on k_{ECM} (through a linear spring relation) and hence is *non-*
115 *mechanosensitive*, is one of the major results of this paper.

116 The active contractile displacement, $\Delta(t)$, which is independent of k_{ECM}, features generic properties
117 that are cell line independent, but also quantitative differences between cell lines. In all cell lines, $\Delta(t)$
118 exhibits a gradual increase with time, until a plateau is reached on a time scale of 5-10 minutes. The exact
119 time to reach the plateau and the plateau level itself do depend on the cell line (Fig. 2C). Moreover, while
120 WT-MEFs and pax-GFP cells often released the pillars (i.e. decrease of the displacement/force) shortly
121 after reaching the plateau, α-act KD and MDA-MB231 cells maintained the pillar displacements for much
122 longer periods (tens of minutes on average) (Fig. 2B), and REF52 often showed a second increase in $\Delta(t)$
123 several minutes after reaching the plateau (Supplementary Fig. 3).

124 **Non-mechanosensitive contractile displacements are directly related to the time-dependent**
125 **concentration of F-actin**

126 The most outstanding questions emerging from the findings presented above are related to the origin
127 of the non-mechanosensitive, intrinsic time-dependent contractile displacement $\Delta(t)$, in particular, its
128 typical time scale and plateau level. Since myosin motors drive contractile force generation, it is logical
129 to assume that the displacement timescales and plateau levels are controlled by the gradual increase in
130 myosin activity. However, myosin is constantly activated and recruited to actin filaments at the cell edge[18],
131 and, moreover, myosin motors generate a quantum of contractile displacement (the working stroke size)
132 on a time scale of milliseconds[15], orders of magnitude faster than the time scale characterizing $\Delta(t)$. This
133 may suggest that it is not the myosin motors per se, but rather the structural evolution of the actin network,
134 to which the myosin motors attach, that might underlie $\Delta(t)$. Thus, we turned to characterize the evolution
135 of the actin networks during force generation using the simplest quantity, i.e. the local (near pillar)
136 concentration (number density) of F-actin, $C_{F-actin}(t)$.

137 To that end, we used three of the five original cell lines that expressed the F-actin reporter tdTomato-
138 tractin[19] – WT MEFs, α-act KD cells, and MDA-MB-231 cells – and performed pillar displacement assays
139 in parallel to tracking the fluorescence level of tractin around each pillar over time, which is a measure
140 of $C_{F-actin}(t)$ (Fig. 3A). As the contractile displacement features a characteristic time of ~10 min (cf. Fig.
141 2B), short time variations in $\delta_{ECM}(t)$ and $C_{F-actin}(t)$ were smoothed out (see Methods); as shown in Fig.
142 3B, both curves appear highly correlated at all times. In fact, $\delta_{ECM}(t)$ and $C_{F-actin}(t)$ of *individual pillars*

143 are highly correlated across the different cell lines and rigidities, as shown in Fig. 3C. To test whether this
144 relation persists to shorter time scales, we analyzed the $C_{F-actin}(t)$ on $\delta_{ECM}(t)$ data without any
145 smoothing (Fig. 3D). The results reveal that both $C_{F-actin}(t)$ and $\delta_{ECM}(t)$ *synchronously oscillate*
146 approximately every 4 minutes, regardless of cell type (Fig. 3E). In >80% of the cases when a rise in
147 displacement was observed, it was accompanied by a simultaneous rise in $C_{F-actin}$. Remarkably, the
148 slightest increase in F-actin density was paralleled by an increase in the contractile displacement, and
149 moreover, short-time scale disassembly of F-actin (decrease in tractin intensity) was paralleled by a drop
150 in displacement (Fig. 3D, Supplementary Fig. 4). These results were further substantiated by experiments
151 in which $C_{F-actin}(t)$ has been significantly and promptly reduced using the actin polymerization inhibitor
152 Latrunculin A, leading to the disappearance of contractile displacements, $\Delta(t) \rightarrow 0$ (Supplementary Fig.
153 5).

154 Taken together, these observations support the simple yet quite remarkable relation:

155 $$d\Delta/dt \sim dC_{F-actin}/dt \quad , \tag{2}$$

156 which suggests that the density of actin filaments essentially determines the contractile displacement
157 generated by the actomyosin network. This implies, as hypothesized above, that myosin motors are not
158 the rate-limiting factor in contractile force generation, i.e. that there are enough of them available at any
159 point in time and that once attachment sites on the actin filaments are available, the myosin motors attach
160 to them and generate displacement rapidly. This picture predicts that the densities of F-actin and myosin
161 motors are highly correlated at any point in time, independently of ECM rigidity.

162 To test this prediction, we seeded cells on the pillar arrays with the two extreme rigidities (2 and 31
163 pN/nm) and fixed them after 30 min, during the contractile phase of spreading[20]. We then stained the cells
164 for F-actin and for phosphorylated (activated) myosin light chain (p-myosin). Using super-resolution
165 microscopy[21], we observed large (micron-scale) actin structures between the pillars, which we classified
166 as network-associated filaments, and small (nanometer-scale) unstructured filaments (Supplementary Fig.
167 6A,B). p-Myosin was arranged in clusters, consistent with the appearance of myosin mini-filaments[12,22]
168 (Supplementary Fig. 6C). We then tested the correlation between the density of the large F-actin structures
169 and p-myosin between the pillars and found high positive correlation regardless of rigidity and cell type
170 (correlation coefficients 0.6-0.7 in all cases; Fig. 3F), as predicted. Since each pillar in the collected images
171 represents a different point in time during the displacement process, this indicates that whenever actin
172 filaments are available, myosin motors operate on them.

173 **Cell-type dependence arises from structural differences in the actin cytoskeleton**

174 The dependence of $\Delta(t)$ on $C_{F-actin}(t)$ implies that any possible cell-type dependence is encapsulated
175 in the proportionality factor in Eq. (2). To test this, we measured the rate of change of $C_{F-actin}(t)$ and of
176 $\delta_{ECM}(t)$ (which measures $\Delta(t)$) during the simultaneous short-time oscillations, and plotted the average
177 $d\delta_{ECM}/dt$ and $dC_{F-actin}/dt$ against each other to extract the proportionality factor. Note that by
178 measuring the relative changes in F-actin concentration, we could disregard any differences in tractin
179 transfection efficiency and in F-actin levels between cells. The resulting graphs indeed exhibit cell-type
180 dependence; in particular, the proportionality factor of MDA-MB231 is significantly higher than that of
181 the other two cell lines (Fig. 4A). This finding indicates that the degree to which the displacements follow
182 changes in F-actin density varies between cell types.

183 To shed light on this cell-type dependence, we utilized the super-resolution images of F-actin and p-
184 myosin to characterize the assembled networks in WT MEF, α-act KD, and MDA-MB-231 cells
185 (Supplementary Fig. 6). We found that across the three cell lines, actin at the cell edges between pillars
186 assembled into networks that occupied similar areas (0.2-0.35 μm^2 per network) and similar complexity
187 of branching (Supplementary Fig. 6D). Interestingly, the number of p-myosin clusters per network in
188 MDA-MB-231 cells was 30-40% lower than the other two cells lines (Supplementary Fig. 6E), possibly
189 related to the relatively low displacement rate of MDA-MB-231 cells (Fig. 2C). This, however, cannot
190 explain the higher proportionality factor in Eq. (2) observed for MDA-MB-231 cells compared to the other
191 cell lines, cf. Fig. 4A. The cell-type dependence of the proportionality factor instead implies that the degree
192 to which changes in $C_{F-actin}$ are translated into contractile displacement depends upon the geometrical
193 properties of the assembled actin network. Indeed, analysis of the spatial organization of F-actin in the
194 cells (Fig. 4B) revealed that whereas MDA-MB-231 cells display highly dense networks, WT MEFs
195 typically form long, parallel, and more highly spaced filaments (Fig. 4C,D) (α-act KD cells were similar
196 to WT MEFs, not shown). Thus, although additional work is required to quantitatively relate the geometry
197 of assembled networks to the proportionality factor, the observed structural differences are likely to be
198 related to the different proportionality factor in Eq. (2) of WT MEFs and α-act KD cells (i.e. different
199 effective force transmission in response to changes in $C_{F-actin}$).

200 **Predictions for well-spread cells in steady-state and consistency with existing literature**

201 The experiments described above were performed on adherent cells that had not yet reached their well-
202 spread steady-state with mature actin stress fibers that span a sizable area of the cell[23]. On the other hand,

our coarse-grained model makes no explicit reference to the specific actin structures that mediate the contractile displacement. Consequently, we expect the model to remain valid also for well-spread cells in steady state. To test this prediction, we used REF52 cells, which were previously shown to generate large forces at steady-state[13], and allowed them to attach to the pillars for 4 hours before imaging. These measurements showed that as in the case of early spreading, $\delta_{ECM}(t)$ generated by well-spread REF52 cells collapses on a master curve that is rigidity-independent (Fig. 5A), strongly supporting the generality of our results. The time-dependent displacement featured a similar time scale (~10 min) in both the steady-state (Fig. 5A) and early spreading (Fig. 2B) regime, possibly suggesting that the contractile displacement $\Delta(t)$ in the two regimes are intrinsically related. To test this, we plot one against the other in Fig. 5B. The result reveals that the two are (predominantly) linearly related to one another, demonstrating that the generated time-dependent displacement in the two regimes is in fact the *very same* function multiplied by a constant (the slope of the linear relation). The slope indicates that the early spreading displacements are 6-7-fold smaller than $\delta_{ECM}(t)$ of the cells at steady state. This may imply that at steady state, when the cell edge extends and forms a new adhesion on a previously non-displaced pillar, the actin filaments that emanate from the new adhesion connect to pre-assembled stress fibers. Indeed, the deflected pillars in these cells were connected to thick actin stress fibers (Fig. 5C, Supplementary Fig. 7) that were not observed in the early stages of spreading (Fig. 5D) (see also Supplementary Note 2).

This remarkable generality is also consistent with the previous results of Trichet et al.[13], who reported $F(t, k_{ECM})$ for cells under well-spread steady state conditions over a broad range of pillars rigidities k_{ECM}. To show this, we first plot $\frac{F(t,k_{ECM})}{k_{ECM}} = \delta_{ECM}(t)$ of Trichet et al.[13] in Supplementary Fig. 8A-B, observing a collapse on a single master curve, as we predict and in agreement with our data in Fig. 5A. Moreover, in Supplementary Fig. 8C we plot our $\delta_{ECM}(t)$ (Fig. 5A) against that of Trichet et al.[13] (Supplementary Fig. 8B), which once more reveals a linear relation, indicating that it is again the very same time-dependent contractile displacement (here, as both measurements were conducted under steady-state conditions, the slope is small, slightly below 2). Consequently, we conclude that cellular contractility under well-spread steady-state conditions is controlled by the very same intrinsic (non-mechanosensitive) displacement $\Delta(t)$, lending strong support to the generality of the emerging picture.

These results in the steady-state regime may have another intriguing implication. The independence of the intrinsic time-dependent contractile displacement $\Delta(t)$ on the rigidity k_{ECM} implies that $\Delta(t)$ is in fact also independent of the length of the stress fibers that are attached to the pillars through focal adhesions.

This is immediately inferred from the clear dependence of the cell size, and consequently of the length of stress fibers, on the rigidity k_{ECM} as observed in Fig. 4 of Trichet et al.[13]. On the other hand, one may assume that like in muscle cells[24,25], myosin II motors apply their contractile displacement everywhere along the stress fiber, implying that $\Delta(t)$ increases with the length of the stress fiber. Our results (as well as those of Trichet et al.[13]) indicate that this is not the case, but rather that stress fibers of different lengths generate the *very same* contractile displacement $\Delta(t)$. This leads to the *activity localization hypothesis,* which suggests that myosin II motors apply their contractile displacement to a rather localized region of the stress fiber, and that the size of this region does not depend on the overall length of the stress fiber.

Discussion

Our results reveal basic aspects of cellular force generation and mechanosensitivity, providing a novel framework to address various questions related to these important cellular processes. The starting point for our investigation is the widespread view that cellular contractile forces are mechanosensitive, i.e. that cells regulate these forces through sensing the rigidity of the ECM. This view is based on previous extensive observations that show that contractile forces depend on ECM rigidity: the larger the rigidity is, the larger cellular contractile forces are[13,26-28]. We show that cellular forces are generated through intrinsic non-mechanosensitive contractile displacements. That is, independently of the ECM rigidity, a particular cell type applies a well-defined time-dependent displacement to its environment (Fig. 2). This implies that the contractile force that is required to reach a certain displacement is proportional to the ECM rigidity, but that this dependence is purely mechanistic, i.e. resulting from a simple linear (Hookean) force-rigidity relation. Consequently, cellular contractile forces are themselves non-mechanosensitive.

These findings have major implications for our understanding of cellular force generation and mechanosensitivity. They show that while contractile cellular forces are not mechanosensitive, information about ECM rigidity is simply encoded in them. Hence, any mechanosensitive cellular process should be sensitive to the contractile force (e.g. its instantaneous magnitude or time rate of change), feeding back the rigidity information into other cellular processes. Moreover, as our findings show that the non-mechanosensitive force generation process emerges from intrinsic time-dependent displacements, any attempt to understand cellular force generation should focus on the intrinsic time-dependent displacements. As a first step towards achieving this important goal, we showed that the time-dependent

262 contractile displacement is directly and universally related to the time evolution of actomyosin networks.
263 In particular, it is shown to be causally related to the density of the actin filaments near the adhesion sites,
264 and the degree to which changes in this density are translated into displacement is shown to depend on the
265 cell-type specific spatial organization and structure of the networks formed by these filaments (Figs. 3-4).

266 Our results reveal a large degree of universality in the time-dependent contractile displacement. In
267 particular, we show that very different cellular states – those pertaining to the early spreading process and
268 those pertaining to steady-state spreading conditions – give rise to essentially the very same time-
269 dependent contractile displacement, differing only by an overall amplitude (Fig. 5). These results are fully
270 consistent with the experimental results of Trichet et al.[13], whose reanalysis also demonstrated non-
271 mechanosensitive contractile displacements that differ by only a multiplicative constant from our own
272 measurements in the well-spread steady-state (for the same cell type, here REF52). Our results also
273 strongly support the relation $k_{Act} \gg k_{ECM}$ (used to derive Eq. (1)), which indicates that over a broad range
274 of conditions, the actin structures involved in the force generation process are much stiffer than the ECM
275 and do not deform at all during the process. This is consistent with previous *in vitro* measurements that
276 showed that actin networks can be up to 40-fold stiffer than the loads that they bear[29].

277 The biophysical picture emerging from our findings is consistent with other available observations in
278 the literature, and hence provide a unifying picture of cellular contractility. For example, while the inferred
279 relation $k_{Act} \gg k_{ECM}$ is relevant to a broad range of physiological conditions, experiments performed on
280 cells adhering to ultra-stiff substrates (e.g. plastic/glass) are in the opposite regime of $k_{Act}(t, k_{ECM}) \ll$
281 k_{ECM}. Under these conditions, where the ECM cannot be deformed, we predict that the displacement $\Delta(t)$
282 is accommodated by stretching the actin structures, $\delta_{Act}(t) \approx \Delta(t) > 0$. Indeed, in laser ablation
283 experiments applied to cells adhering to glass plates[30], stress fibers are observed to instantaneously retract
284 by an amount comparable to the saturation level of $\delta_{ECM}(t \to \infty) \approx \Delta(t \to \infty)$ observed in Fig. 5A and
285 Supplementary Fig. 8B (see also Supplementary Note 2). This observation further supports the major
286 result that the contractile displacement $\Delta(t)$ is an intrinsic, non-mechanosensitive property of cells
287 (independently of ECM rigidity, and independently of whether the displacement is accommodated by the
288 ECM or by F-actin structures). It is important to stress that our use of ECM pillars whose effective rigidity
289 varies with their height alone, keeping their material and surface properties entirely fixed, enables us to
290 cleanly isolate the effect of the external rigidity, ruling out any possible intervening surface chemistry
291 effects.

Previous studies of force regulation as a function of ECM rigidity have given rise to the 'integrin clutch model', which predicts that contractile forces depend on the number of attached clutches (integrins) to the moving, polymerization-driven, actin fibers[31-33]. Our results show that the non-mechanosensitive contractility critically depends on the density of F-actin, as well as its spatial organization, making no explicit reference to the polymerization-driven flow of actin. As we have not measured the number of engaged clutches at each time-point during the contractile displacement process (nor is it possible to the best of our knowledge to accurately perform such measurements), the relation between the density of F-actin and adhesion dynamics should be further explored (e.g. in light of the common view that F-actin is recruited at the adhesion sites).

Our findings also give rise to various important questions. First, there is a need to go beyond the discovered $d\Delta(t)/dt \sim dC_{F-actin}(t)/dt$ relation, which in itself should be further studied, in order to understand the origin of some of the properties of $\Delta(t)$. In particular, the activity localization hypothesis associated with $\Delta(t)$ should be further tested in future work, together with the origin of the characteristic time scale and plateau levels of $\Delta(t)$, including their cell-type dependence. In addition, the mechanism behind the short-time oscillatory behavior of F-actin (characterized by a time of ~4 min) should be clarified, potentially in relation to the cyclic activation/de-activation of actin polymerization factors, as was recently observed in contracting secretory vesicles[34]. The relation between this oscillatory time scale and the lifetime of adhesions, during force loading[35,36], including the turnover time of proteins within them, should be further explored. Finally, our main result, $F(t, k_{ECM}) \approx k_{ECM}\,\Delta(t)$, shows that mechanosensing is driven by cells through $\Delta(t)$ and that the sensing itself is done through the contractile force $F(t, k_{ECM})$. How the latter feeds back into various internal cellular processes should be further explored with particular focus on the time-dependent accumulation of rigidity signals, rather than exclusively on their magnitude. This may shift our view of mechanosensitivity toward the dynamic nature of this process.

317 # Methods

318 **Cells culture and reagents**

319 WT MEFs (RPTPα$^{+/+}$ cells[37]) and α-act KD MEFs[38] were a kind gift from Mike Sheetz (Columbia
320 University & MBI Singapore). REF52 cells[39] and pax-GFP cells (Ilk$^{f/f}$ fibroblasts stably expressing
321 paxillin–EGFP[40]) were a kind gift from Benny Geiger (Weizmann Institute of Science). MDA-MB-231
322 cells[41] were a kind gift from Yuval Shaked (Technion). All cells were cultured at 37° C in a 5% CO2
323 incubator in Dulbecco's Modified Eagle Medium (DMEM) supplemented with 10% fetal bovine serum,
324 and 100 IU/ml Penicillin-Streptomycin (all reagents were from Biological Industries).

325 **Plasmids and transfections**

326 The YFP-Tpm2.1 plasmid was a kind gift from Peter Gunning (The University of New South Wales).
327 The tdTomato-tractin plasmid was a kind gift from Mike Sheetz (Columbia University & MBI Singapore).
328 Transfections were carried out 1 day before measurements using the NEPA21 Electroporator (Nepa Gene)
329 according to the manufacturer's instructions, with ~10^6 cells per reaction and 10 µg DNA.

330 **Pillar and soft gel fabrication**

331 In the pillar experiments, the external rigidity k_{ECM} is controlled by varying the height of the pillars,
332 while keeping their cross-sectional area and intrinsic chemical properties fixed. All pillars had a diameter
333 of 2 µm, and heights of 5.3, 9.4, or 13.2 µm. We used 2 µm diameter pillars as these can be used to
334 measure the long-term time-dependent forces that are generated after initial formation and reinforcement
335 of the adhesions[10,12]. The center-to-center spacing between pillars was 4 µm. Pillar bending stiffness,
336 k_{ECM}, was calculated by Euler–Bernoulli beam theory:

337 $$k_{ECM} = \frac{3\pi}{64}\frac{ED^4}{L^3}$$

338 where D and L are the diameter and length of the pillar, respectively, and E is the Young's modulus of
339 the material (=2 MPa for the PDMS used here).

340 Using a common relation to estimate an effective elastic modulus that corresponds to a given rigidity
341 $E_{eff} = \frac{9k_{ECM}}{4\pi a}$, where a is the radius of the pillars[42], we obtain effective elastic moduli in the range $E_{eff} \approx$
342 $1.5 - 22$ kPa. The latter is well within the relevant physiological regime, ranging from endothelial tissues
343 to cartilage[17], thus allowing us to test the relevance of the relation $k_{Act}(t, k_{ECM}) \gg k_{ECM}$ to a broad range
344 of physiological conditions.

345 Pillar fabrication was done by pouring PDMS (mixed at 10:1 with its curing agent, Sylgard 184; Dow
346 Corning) into silicon molds (fabricated as previously described[10]) with holes at fixed depths and distances.

347 The molds were then placed, face down, onto glass-bottom 35 mm dishes (#0 coverslip, Cellvis) which
348 were incubated at 65°C for 12h to cure the PDMS. The molds were next peeled off while immersed in
349 ethanol to prevent pillar collapse. The ethanol was replaced with PBS, and human plasma full-length
350 fibronectin (Merck) was added to the dish at a final concentration of 10 μg/μl for a 1h incubation at 37°C.
351 Next, residual fibronectin was washed away by replacing the buffer to HBSS buffer (Biological Industries)
352 supplemented with 20 mM HEPES (pH 7.2).

353 1 and 40 kPa substrates (Supplementary Fig. 1) were fabricated by using Sylgard 52-276, at a ratio of
354 1:1.1 and 1:3.2, respectively, according to the measurements performed by Ou et al.[43].

355 **Pillar displacement measurements**

356 One day prior to the pillar experiments, cells were sparsely plated to minimize cell-cell interactions
357 prior to re-plating. The following day, cells were trypsinized, centrifuged with growth medium, and then
358 resuspended and pre-incubated in HBSS/Hepes at 37°C for 30 min prior to the experiment. Cells were
359 then spread on the fibronectin-coated pillars. In all cases, we made sure that the cells were isolated when
360 plated on the substrates.

361 Time-lapse imaging of cells spreading on the pillars was performed using an inverted microscope
362 (Leica DMIRE2) at 37°C using a 63x 1.4 NA oil immersion objective. Brightfield images were recorded
363 every 10 seconds with a Retiga EXi Fast 1394 CCD camera (QImaging). The microscope and camera
364 were controlled by Micromanager software[44]. For each cell, a movie of 1-3 hours was recorded. To
365 minimize photo-damage to the cells, a 600 nm longpass filter was inserted into the illumination path.

366 Tracking of pillar movements over time was performed with ImageJ (National Institutes of Health)
367 using the Nanotracking plugin, as described previously[12]. In short, the cross-correlation between the pillar
368 image in every frame of the movie and an image of the same pillar from the first frame of the movie was
369 calculated, and the relative x- and y-position of the pillar in every frame of the movie was obtained. To
370 consider only movements of pillar from their zero-position, we only analyzed pillars that at the start of the
371 movie were not in contact with the cell and that during the movie the cell edge reached to them. Drift
372 correction was performed using data from pillars far from any cell in each movie. For each pillar, the
373 displacement curve was generated by Matlab (MathWorks).

374 Parallel measurements of tdTomato-tractin intensity and pillar displacements were performed on a
375 Zeiss LSM800 confocal microscope using a 63x 1.4NA objective at 37°C. Images were taken every 30
376 seconds and measurements of pillar movements were performed as described above. Measurements of
377 tdTomato-tractin intensity were taken around each pillar of interest in a circular area with a radius of 2μm.

Smoothing of the data in Fig. 3B was done using a moving average with a window size of 30 frames (5 minutes).

Analyses of correlation between changes in F-actin density and in pillar displacement during the short-term oscillations (Fig. 3D) were performed only on displacements that began below the noise level (~20nm).

Fluorescence microscopy

For immunofluorescence microscopy, cells were plated on fibronectin-coated pillars, fixed with 4% paraformaldehyde, and permeabilized with 0.1% Triton X-100. Immunolabeling was performed with primary antibodies against p-myosin (Abcam) overnight at 4°C, and with Alexa-488 or Alexa-555-conjugated secondary antibodies for 1 h at room temperature. Images were taken with a Zeiss LSM800 confocal microscope using a 63x 1.4NA objective.

For super-resolution analyses (Super-Resolution Radial Fluctuations; SRRF[21]), a region of interest (ROI) of 12µm x 12µm was imaged using the Airyscan function on the LSM800 confocal microscope. A series of 25 images was taken at 5fps; these were processed using the Airyscan algorithm using the ZEN blue software (Zeiss), followed by further processing using the SRRF algorithm[21]. The trainable Weka segmentation plugin for FIJI[45] was then used to define the actin fibers between the pillars (Fig. 4), and thresholding was used to define the p-myosin clusters above background fluorescence levels. Fiber orientation analysis was done using the Ridge Detection and OrientationJ plugins for FIJI.

Statistical analysis

Matlab (MathWorks) was used for data analysis and graph plotting. All ensemble average pillar displacement curves are shown with error bars representing the standard error of the mean (SEM). In the boxplots displayed in the figures the central mark indicates the median, the bottom and top edges of the box indicate the 25th and 75th percentiles, respectively, and the whiskers extend to the most extreme data points not considered outliers; outliers are not shown.

Acknowledgments

We are grateful to Yuri Lubomirsky (Weizmann Institute of Science) for discussions related to Eq. (1), to Noam Kaplan (Technion – Israel Institute of Technology) for discussions on data analysis, and to Sasha Bershadsky (Mechanobiology Institute, Singapore) for discussions related to theoretical aspects of this work. H.W. acknowledges support from the Israel Science Foundation (1738/17) and from the Rappaport Institute. H.W. is an incumbent of the David and Inez Myers Career Advancement Chair in Life Sciences.

E.B. acknowledges support from the William Z. and Eda Bess Novick Young Scientist Fund and from the Harold Perlman Family.

Author contributions

L.F. performed the experiments and analyzed the data; L.K. and A.M. assisted in data analysis and pillar experiments, respectively; A.L. and E.B. conceived and developed the theory; E.B and H.W. conceived and planned the experiments; E.B. and H.W. wrote the manuscript. All authors discussed the results and contributed to the final manuscript.

Conflict of interest statement: The authors declare no competing financial interest.

References

1 Iskratsch, T., Wolfenson, H. & Sheetz, M. P. Appreciating force and shape-the rise of mechanotransduction in cell biology. *Nat. Rev. Mol. Cell Biol.* **15**, 825-833, doi:10.1038/nrm3903 (2014).

2 Lo, C. M., Wang, H. B., Dembo, M. & Wang, Y. L. Cell movement is guided by the rigidity of the substrate. *Biophys. J.* **79**, 144-152, doi:10.1016/S0006-3495(00)76279-5 (2000).

3 O'Connor, J. W., Riley, P. N., Nalluri, S. M., Ashar, P. K. & Gomez, E. W. Matrix Rigidity Mediates TGFbeta1-Induced Epithelial-Myofibroblast Transition by Controlling Cytoskeletal Organization and MRTF-A Localization. *J. Cell Physiol.* **230**, 1829-1839, doi:10.1002/jcp.24895 (2015).

4 Prager-Khoutorsky, M. *et al.* Fibroblast polarization is a matrix-rigidity-dependent process controlled by focal adhesion mechanosensing. *Nat. Cell Biol.* **13**, 1457-1465, doi:10.1038/ncb2370 (2011).

5 Saez, A., Ghibaudo, M., Buguin, A., Silberzan, P. & Ladoux, B. Rigidity-driven growth and migration of epithelial cells on microstructured anisotropic substrates. *Proc. Natl. Acad. Sci. USA* **104**, 8281-8286, doi:10.1073/pnas.0702259104 (2007).

6 Wang, H. B., Dembo, M. & Wang, Y. L. Substrate flexibility regulates growth and apoptosis of normal but not transformed cells. *Am. J. Physiol Cell Physiol.* **279**, C1345-1350 (2000).

7 Chaudhuri, O. *et al.* Extracellular matrix stiffness and composition jointly regulate the induction of malignant phenotypes in mammary epithelium. *Nat Mater* **13**, 970-978, doi:10.1038/nmat4009 (2014).

8 Doyle, A. D. *et al.* Micro-environmental control of cell migration--myosin IIA is required for efficient migration in fibrillar environments through control of cell adhesion dynamics. *J. Cell Sci.* **125**, 2244-2256, doi:10.1242/jcs.098806 (2012).

9 Provenzano, P. P., Inman, D. R., Eliceiri, K. W. & Keely, P. J. Matrix density-induced mechanoregulation of breast cell phenotype, signaling and gene expression through a FAK-ERK linkage. *Oncogene* **28**, 4326-4343, doi:10.1038/onc.2009.299 (2009).

10 Ghassemi, S. *et al.* Cells test substrate rigidity by local contractions on submicrometer pillars. *Proc. Natl. Acad. Sci. USA* **109**, 5328-5333, doi:1119886109 [pii] 10.1073/pnas.1119886109 (2012).

11 Elosegui-Artola, A. *et al.* Mechanical regulation of a molecular clutch defines force transmission and transduction in response to matrix rigidity. *Nat. Cell Biol.* **18**, 540-548, doi:10.1038/ncb3336 (2016).

12 Wolfenson, H. *et al.* Tropomyosin controls sarcomere-like contractions for rigidity sensing and suppressing growth on soft matrices. *Nat. Cell Biol.* **18**, 33-42, doi:10.1038/ncb3277 (2016).

13 Trichet, L. *et al.* Evidence of a large-scale mechanosensing mechanism for cellular adaptation to substrate stiffness. *Proc. Natl. Acad. Sci. USA* **109**, 6933-6938, doi:10.1073/pnas.1117810109 (2012).

14 Ghassemi, S. *et al.* Fabrication of elastomer Pillar Arrays with Modulated Stiffness for Cellular Force Measurements. *J Vac Sci Technol B Microelectron Nanometer Struct Process Meas Phenom* **26**, 2549-2553 (2008).

15 Kaya, M. & Higuchi, H. Nonlinear elasticity and an 8-nm working stroke of single myosin molecules in myofilaments. *Science* **329**, 686-689, doi:10.1126/science.1191484 (2010).

16 Schwarz, U. S., Erdmann, T. & Bischofs, I. B. Focal adhesions as mechanosensors: the two-spring model. *Bio Systems* **83**, 225-232, doi:10.1016/j.biosystems.2005.05.019 (2006).

464 17 Cox, T. R. & Erler, J. T. Remodeling and homeostasis of the extracellular matrix: implications
465 for fibrotic diseases and cancer. *Disease models & mechanisms* **4**, 165-178,
466 doi:10.1242/dmm.004077 (2011).
467 18 Shutova, M., Yang, C., Vasiliev, J. M. & Svitkina, T. Functions of nonmuscle myosin II in
468 assembly of the cellular contractile system. *PLoS ONE* **7**, e40814,
469 doi:10.1371/journal.pone.0040814 (2012).
470 19 Belin, B. J., Goins, L. M. & Mullins, R. D. Comparative analysis of tools for live cell imaging of
471 actin network architecture. *Bioarchitecture* **4**, 189-202, doi:10.1080/19490992.2014.1047714
472 (2014).
473 20 Wolfenson, H., Yang, B. & Sheetz, M. P. Steps in Mechanotransduction Pathways that Control
474 Cell Morphology. *Annu. Rev. Physiol.* **81**, 585-605, doi:10.1146/annurev-physiol-021317-
475 121245 (2019).
476 21 Gustafsson, N. *et al.* Fast live-cell conventional fluorophore nanoscopy with ImageJ through
477 super-resolution radial fluctuations. *Nat Commun* **7**, 12471, doi:10.1038/ncomms12471 (2016).
478 22 Lohner, J. *et al.* Large and reversible myosin-dependent forces in rigidity sensing. *Nature*
479 *Physics*, doi:10.1038/s41567-019-0477-9 (2019).
480 23 Burridge, K. & Guilluy, C. Focal adhesions, stress fibers and mechanical tension. *Exp. Cell Res.*
481 **343**, 14-20, doi:10.1016/j.yexcr.2015.10.029 (2016).
482 24 ter Keurs, H. E. The interaction of Ca2+ with sarcomeric proteins: role in function and
483 dysfunction of the heart. *American journal of physiology. Heart and circulatory physiology* **302**,
484 H38-50, doi:10.1152/ajpheart.00219.2011 (2012).
485 25 Livne, A. & Geiger, B. The inner workings of stress fibers - from contractile machinery to focal
486 adhesions and back. *J. Cell Sci.* **129**, 1293-1304, doi:10.1242/jcs.180927 (2016).
487 26 Oakes, P. W. *et al.* Lamellipodium is a myosin-independent mechanosensor. *Proc. Natl. Acad.*
488 *Sci. USA* **115**, 2646-2651, doi:10.1073/pnas.1715869115 (2018).
489 27 Mih, J. D., Marinkovic, A., Liu, F., Sharif, A. S. & Tschumperlin, D. J. Matrix stiffness reverses
490 the effect of actomyosin tension on cell proliferation. *J. Cell Sci.* **125**, 5974-5983,
491 doi:10.1242/jcs.108886 (2012).
492 28 Wu, Z., Plotnikov, S. V., Moalim, A. Y., Waterman, C. M. & Liu, J. Two Distinct Actin
493 Networks Mediate Traction Oscillations to Confer Focal Adhesion Mechanosensing. *Biophys. J.*
494 **112**, 780-794, doi:10.1016/j.bpj.2016.12.035 (2017).
495 29 Bieling, P. *et al.* Force Feedback Controls Motor Activity and Mechanical Properties of Self-
496 Assembling Branched Actin Networks. *Cell* **164**, 115-127, doi:10.1016/j.cell.2015.11.057
497 (2016).
498 30 Russell, R. J., Xia, S. L., Dickinson, R. B. & Lele, T. P. Sarcomere mechanics in capillary
499 endothelial cells. *Biophys. J.* **97**, 1578-1585, doi:10.1016/j.bpj.2009.07.017 (2009).
500 31 Chan, C. E. & Odde, D. J. Traction dynamics of filopodia on compliant substrates. *Science* **322**,
501 1687-1691, doi:10.1126/science.1163595 (2008).
502 32 Elosegui-Artola, A., Trepat, X. & Roca-Cusachs, P. Control of Mechanotransduction by
503 Molecular Clutch Dynamics. *Trends Cell Biol.* **28**, 356-367, doi:10.1016/j.tcb.2018.01.008
504 (2018).
505 33 Case, L. B. & Waterman, C. M. Integration of actin dynamics and cell adhesion by a three-
506 dimensional, mechanosensitive molecular clutch. *Nat. Cell Biol.* **17**, 955-963,
507 doi:10.1038/ncb3191 (2015).

34 Segal, D., Zaritsky, A., Schejter, E. D. & Shilo, B. Z. Feedback inhibition of actin on Rho mediates content release from large secretory vesicles. *J. Cell Biol.* **217**, 1815-1826, doi:10.1083/jcb.201711006 (2018).

35 Wolfenson, H., Bershadsky, A., Henis, Y. I. & Geiger, B. Actomyosin-generated tension controls the molecular kinetics of focal adhesions. *J. Cell Sci.* **124**, 1425-1432, doi:10.1242/jcs.077388 (2011).

36 Lavelin, I. *et al.* Differential effect of actomyosin relaxation on the dynamic properties of focal adhesion proteins. *PLoS ONE* **8**, e73549, doi:10.1371/journal.pone.0073549 (2013).

37 Jiang, G., Huang, A. H., Cai, Y., Tanase, M. & Sheetz, M. P. Rigidity sensing at the leading edge through alphavbeta3 integrins and RPTPalpha. *Biophys. J.* **90**, 1804-1809 (2006).

38 Roca-Cusachs, P. *et al.* Integrin-dependent force transmission to the extracellular matrix by alpha-actinin triggers adhesion maturation. *Proc. Natl. Acad. Sci. USA* **110**, E1361-1370, doi:10.1073/pnas.1220723110 (2013).

39 Cavalcanti-Adam, E. A. *et al.* Cell spreading and focal adhesion dynamics are regulated by spacing of integrin ligands. *Biophys. J.* **92**, 2964-2974 (2007).

40 Elad, N. *et al.* The role of integrin-linked kinase in the molecular architecture of focal adhesions. *J. Cell Sci.* **126**, 4099-4107, doi:10.1242/jcs.120295 (2013).

41 Gingis-Velitski, S. *et al.* Host response to short-term, single-agent chemotherapy induces matrix metalloproteinase-9 expression and accelerates metastasis in mice. *Cancer Res.* **71**, 6986-6996, doi:10.1158/0008-5472.CAN-11-0629 (2011).

42 Ghibaudo, M. *et al.* Traction forces and rigidity sensing regulate cell functions. *Soft Matter* **4**, 1836, doi:10.1039/b804103b (2008).

43 Ou, G. *et al.* Visualizing mechanical modulation of nanoscale organization of cell-matrix adhesions. *Integrative biology : quantitative biosciences from nano to macro* **8**, 795-804, doi:10.1039/c6ib00031b (2016).

44 Edelstein, A., Amodaj, N., Hoover, K., Vale, R. & Stuurman, N. Computer control of microscopes using microManager. *Curr Protoc Mol Biol* ***92***, 14.20.11–14.20.17, doi:10.1002/0471142727.mb1420s92 (2010).

45 Arganda-Carreras, I. *et al.* Trainable Weka Segmentation: a machine learning tool for microscopy pixel classification. *Bioinformatics* **33**, 2424-2426, doi:10.1093/bioinformatics/btx180 (2017).

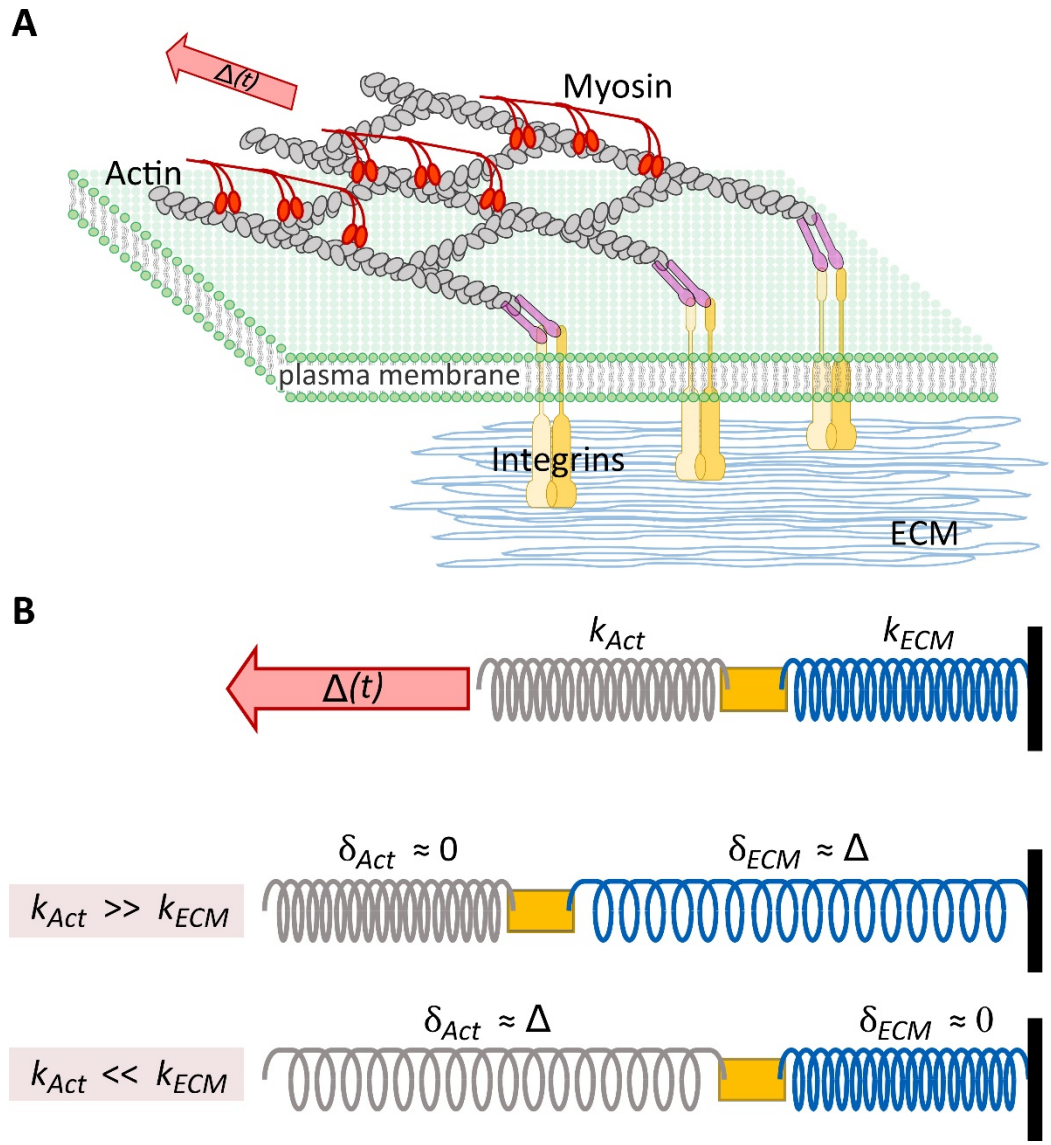

Figure 1. A simple model of cellular contractility. (A) A schematic of the cellular force generation machinery. that Shown are the integrin molecules, which are attached to the ECM at their extracellular side, and to actin structures (indirectly, through adapter proteins – purple rods) at the cellular side. Myosin motors that attach to the actin filaments generate a time-dependent displacement, $\Delta(t)$ (red arrow). (B) Top: An abstraction of panel A in which a spring of effective rigidity k_{ECM}, representing the ECM, is connected in series to another spring of effective rigidity k_{Act}, representing the actin structures. The contractile displacement $\Delta(t)$, which is applied to the actin structures, is also shown. Color code as in panel A. Middle: The degree to which the ECM or the actin structures are deformed depends on their relative rigidity. For $k_{Act} \gg k_{ECM}$, the myosin-generated contractile displacement $\Delta(t)$ is accommodated by ECM deformation, $\delta_{ECM} \approx \Delta$, while the actin filaments composing the actin structures slide past each other as rigid objects with no internal deformation, $\delta_{Act} \approx 0$. Bottom: In the opposite limit (relevant for experiments performed on rigid ECM, e.g. plastic/glass plates), $k_{Act} \ll k_{ECM}$, the myosin-generated contractile displacement $\Delta(t)$ is accommodated by stretching the actin filaments composing the actin structures, $\delta_{Act} \approx \Delta$, while the rigid ECM is not deformed, $\delta_{ECM} \approx 0$.

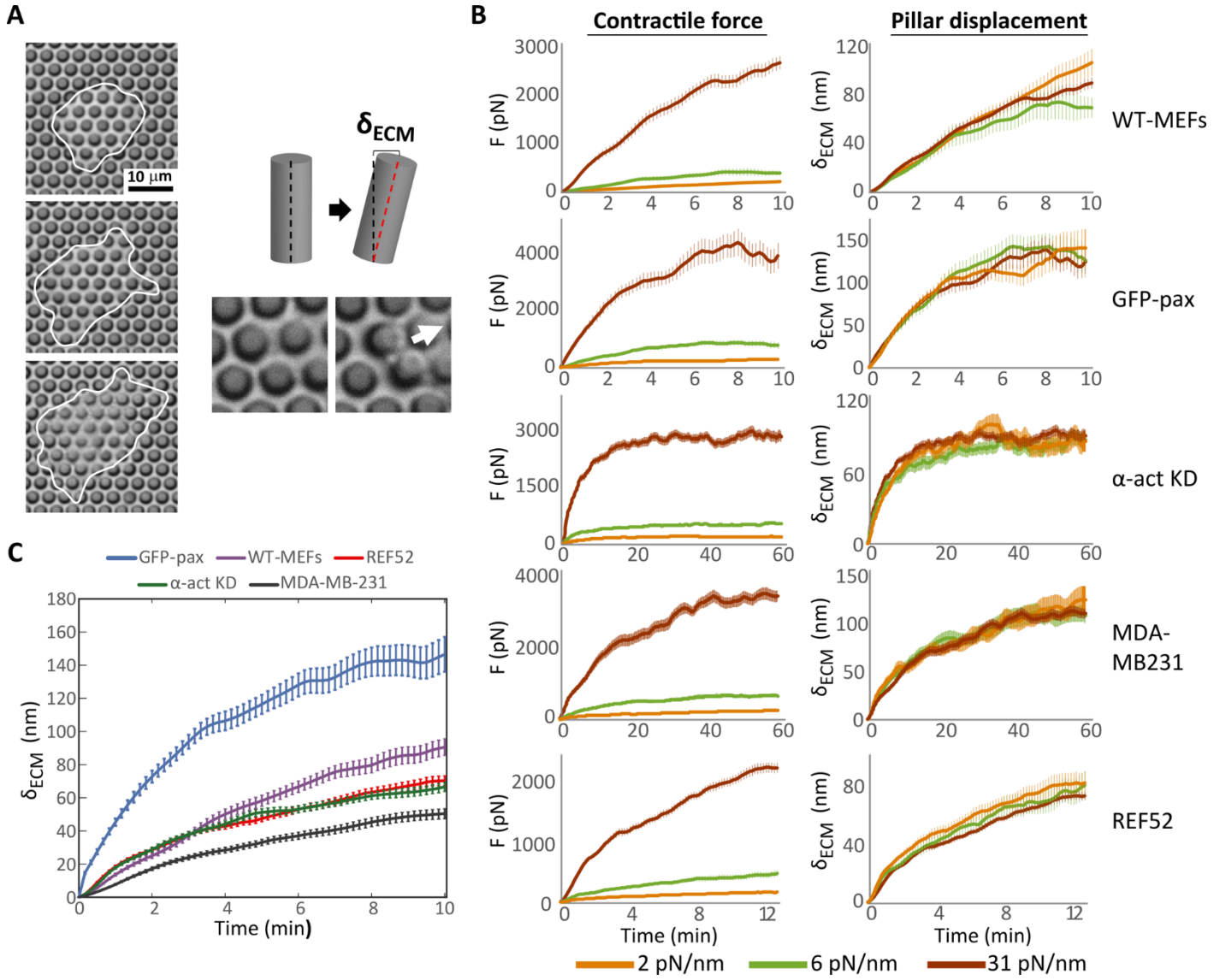

Figure 2. Pillar array experiments reveal a cell-specific, time-dependent, rigidity-independent contractile displacements. We used low-illumination brightfield time-lapse imaging to track live cells for several hours as they spread on the pillars to measure $\delta_{ECM}(t)$. (A) Left: Frames from a time-lapse movie of a mouse fibroblast spreading on an array of 2µm diameter pillars coated with fibronectin (cell borders marked by the white line). Right: When the cell forms adhesions on the pillars, it pulls on them; pillar displacement (δ_{ECM}) can be observed by tracking their tops over time. (B) Mean ± SEM of the time-dependent contractile forces ($F(t, k_{ECM})$, left) and pillar displacement ($\delta_{ECM}(t) = F(t, k_{ECM})/k_{ECM}$, right) on pillars of three widely different rigidities (corresponding to different pillar heights, the rigidity values appear on the legend). For all cell lines tested, $\delta_{ECM}(t) = F(t, k_{ECM})/k_{ECM}$ collapsed onto a single master curve (right). n>50 pillars from >8 cells in each case. (C) Averages of the pillar displacement data from all three rigidities (panel B right) reveal cell-specific contractile displacements.

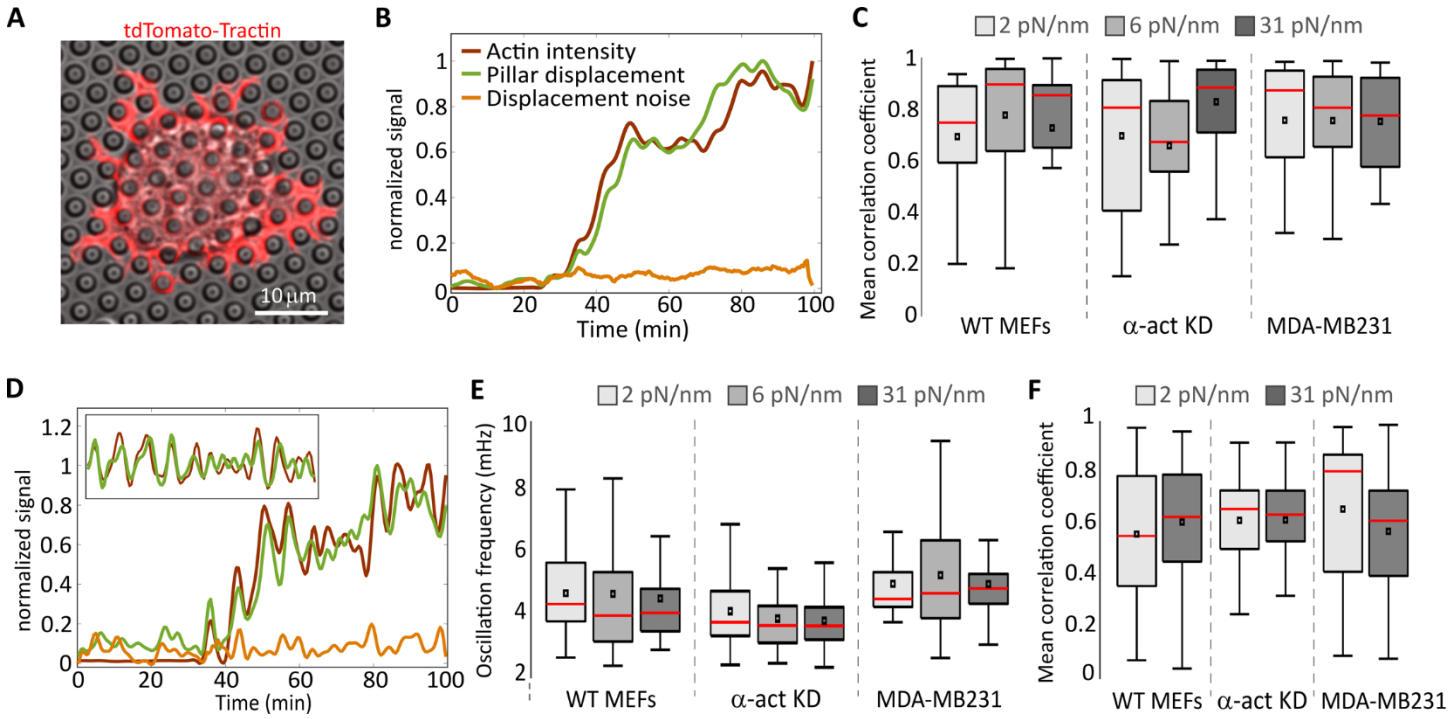

Figure 3. Correlation between F-actin density and pillar displacement. (A) Micrograph of a mouse fibroblast (WT MEF) expressing tdTomato-tractin and spreading on 2µm-diameter pillars. (B) Example of low-pass filtered curves of pillar displacement and of tractin intensity around the same pillar over time. (C) Mean correlation coefficients of pillar displacement and tractin intensity such as in panel B. n>30 from >5 cells in each case. The amplitude of the displacement noise, obtained by measuring the magnitude of the displacement (irrespective of its direction) of a pillar that was not in contact with the cell throughout the experiment, is added for reference. (D) Non-low-pass-filtered pillar displacement and tractin intensity over time curves reveal simultaneous oscillations in both. Inset shows the same data (starting from the initial rise of both signals) after subtraction of the low-pass filter curves in each case (i.e., minus the so-called DC component). Colors are as in panel B (see legend there). (E) Mean frequency of pillar displacement oscillations. The frequency was calculated using Fourier transform. Tractin oscillated at a similar frequency in all cases (not shown). (F) Mean correlation coefficients of actin and myosin density between the pillars.

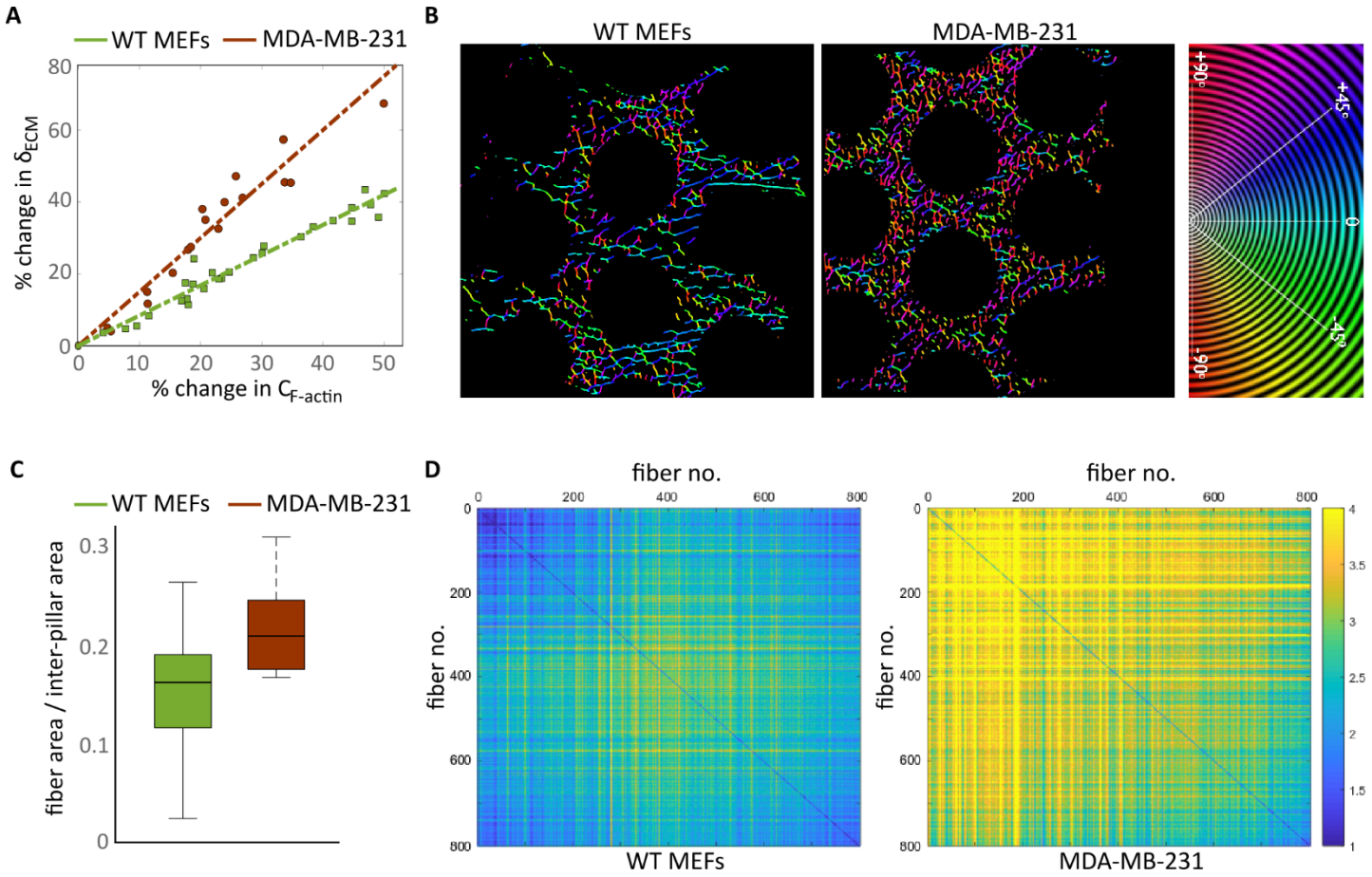

Figure 4. Structural differences in F-actin organization correlate with displacement response to $C_{F-actin}(t)$. (A) The rate of change (in percent) of δ_{ECM}, which quantifies $d\Delta/dt$, as a function of rate of change (in percent) of $C_{F-actin}$, which quantifies $dC_{F-actin}/dt$. Measurements were taken during each rise in the simultaneous oscillations (Fig. 3D), averaged for each rigidity (n>60 data points from >15 pillars from >4 cells in each case), and all data points from all three rigidities are plotted here for WT MEFs and MDA-MB-231 cells. For visual clarity, the α-act KD data (which are closer to those of WT MEFs than to these of MDA-MB-231 cells) are not shown. (B) Processed super-resolution images of large actin filaments at the cell edge color-coded for angles (see Methods for details). Only part of the cell edge is shown in each case; the right side of each image is outside of the cell. α-act KD cells displayed similar fiber distribution to that of WT MEFs (not shown). (C) Ratio between the area occupied by the large actin fibers and the inter-pillar area at the cell edge. MDA-MB-231 networks were ~50% more dense compared to WT MEFs (p-value < 0.001). (D) WT MEFs display highly parallel fibers compared to MDA-MB-231. Images such as those shown in panel B were analyzed as follows: the largest 800 fibers in each image were arranged according to size in ascending order and the inter-fiber slope differences were calculated for each fiber against all other fibers in each image. These differences are represented here by color-coded plots. The images shown are the average of 40 images in each case. Lower values (blue hues) represent parallel fibers. α-act KD showed a similar distribution to that of WT MEFs (not shown).

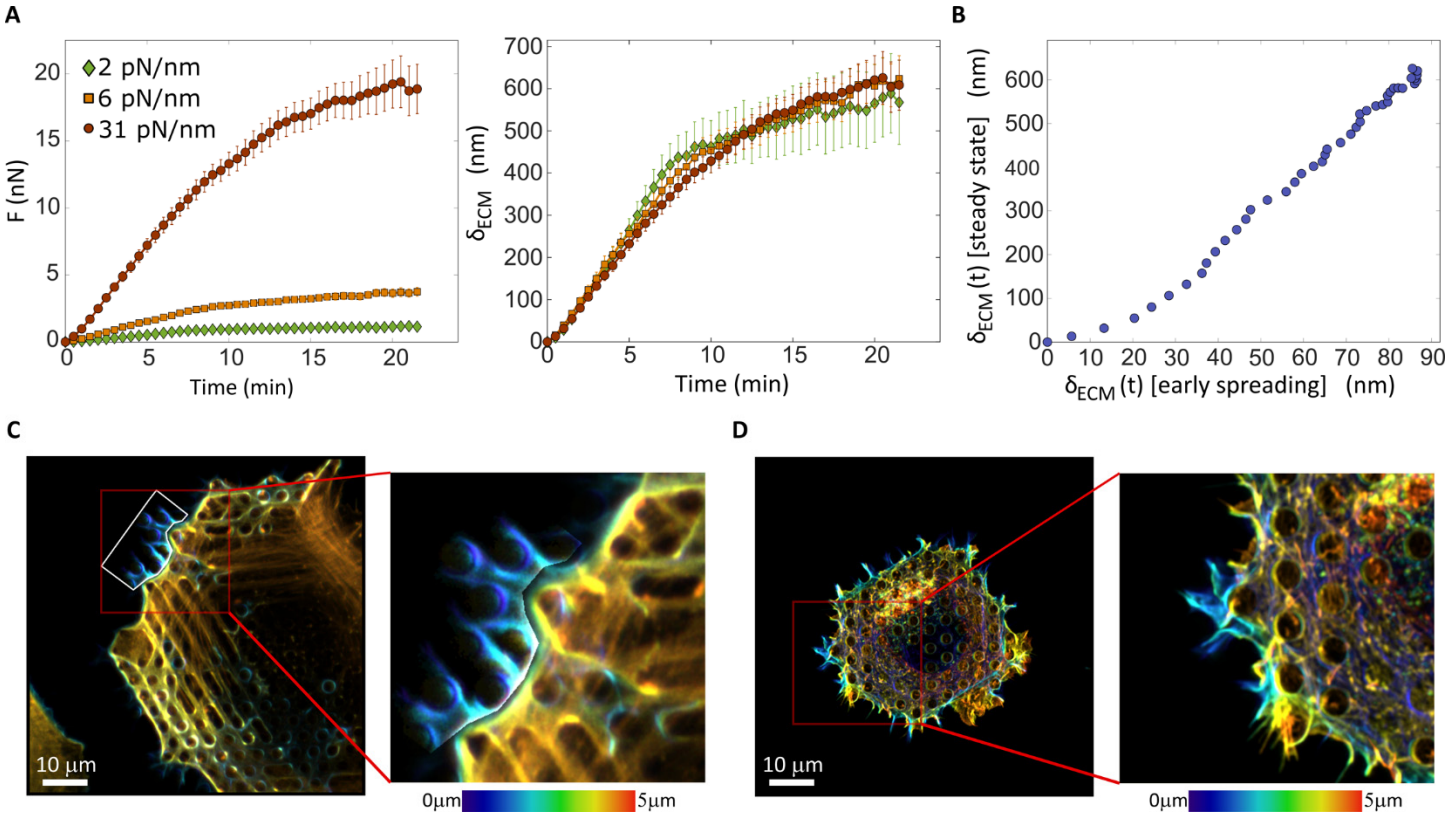

Figure 5. (A) $F(t, k_{ECM})$ and $\delta_{ECM}(t) = F(t, k_{ECM})/k_{ECM}$ curves (left and right, respectively) of REF52 cells under well-spread steady-state conditions. (B) $\delta_{ECM}(t)$ of early spreading REF52 cells (cf. Fig. 2C) vs. $\delta_{ECM}(t)$ of REF52 under well-spread steady-state conditions (panel B). (C-D) Z-stack projections of REF52 cells on 31pN/nm pillars stained for F-actin color-coded for depth; (C) Cell after 5h of spreading. The brightness of the region marked by white borders was enhanced for purpose of clarity. Thick actin stress fibers (yellow-orange hues) are observed 2-4µm above the fibers directly surrounding the pillar (blue hues). (D) Cell after 30min of spreading. No stress fibers are observed and the actin structures are much less organized compared to steady-state condition (panel C).

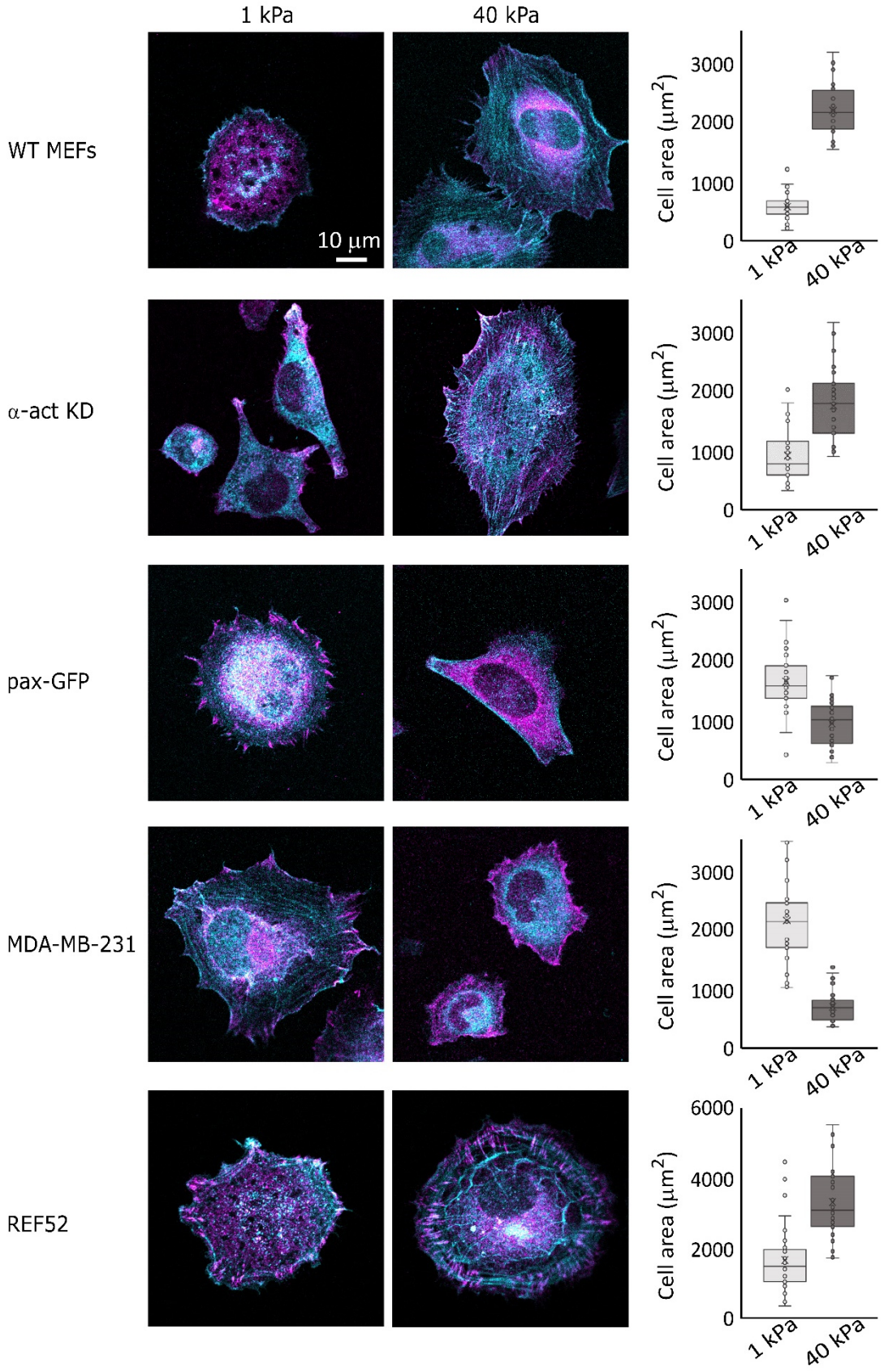

Supplementary Figure 1. Representative images of all 5 cell lines plated on 1 and 40 kPa continuous gels for 3h and stained for vinculin (magenta) and F-actin (cyan). Whereas WT-MEFs, α-act KD cells, and REF52 display larger adhesions and more organized stress fibers on stiff vs. soft, the opposite is observed for pax-GFP cells and MDA-MB-231 cells. The right boxplots show the differences in cell area on the different rigidities (n>30 cells in each case).

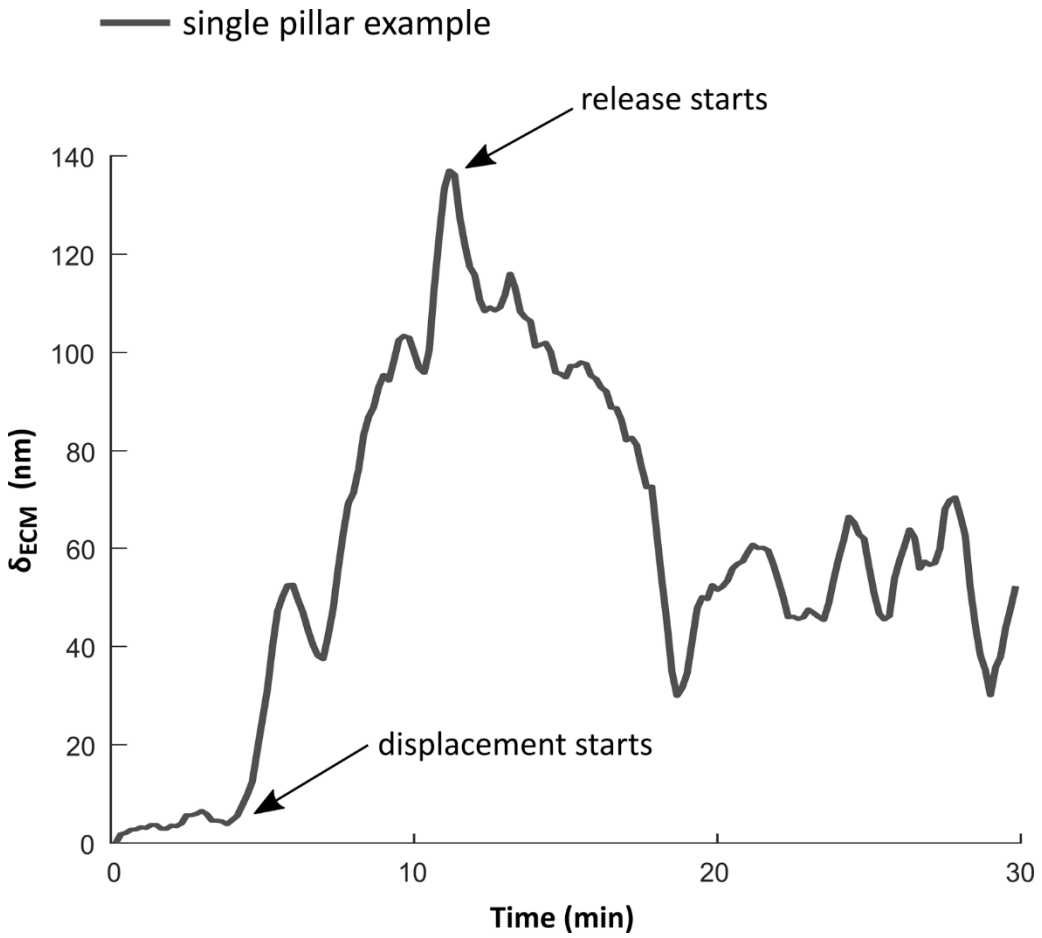

Supplementary Figure 2. Example of a single pillar displacement curve. The beginning of the release was defined by the time point of maximal displacement.

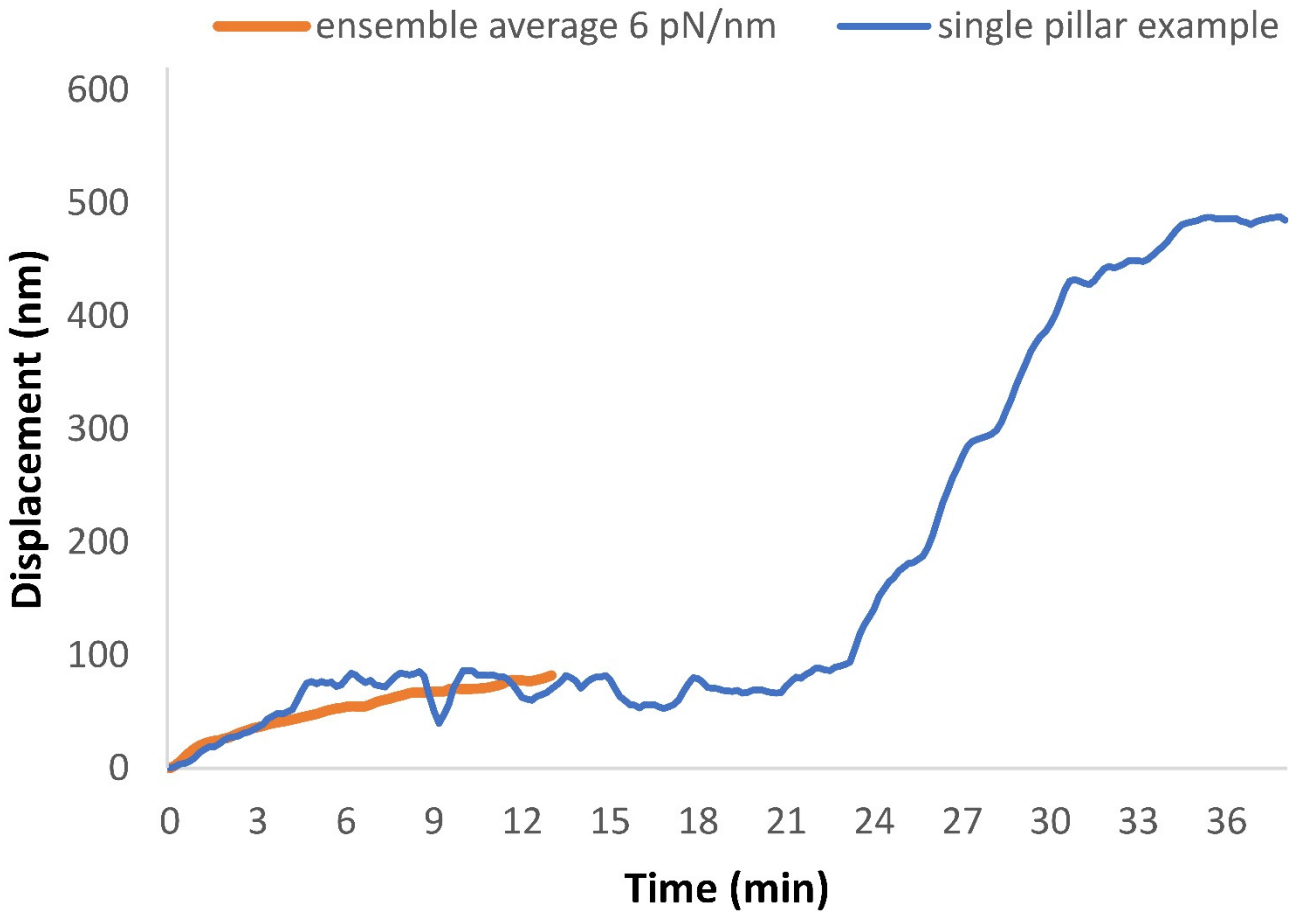

Supplementary Figure 3. Example of a single pillar displacement curve of a REF52 cell showing a second rise in displacement several minutes after an initial plateau was reached. The orange curve is the same as shown in Fig. 2B.

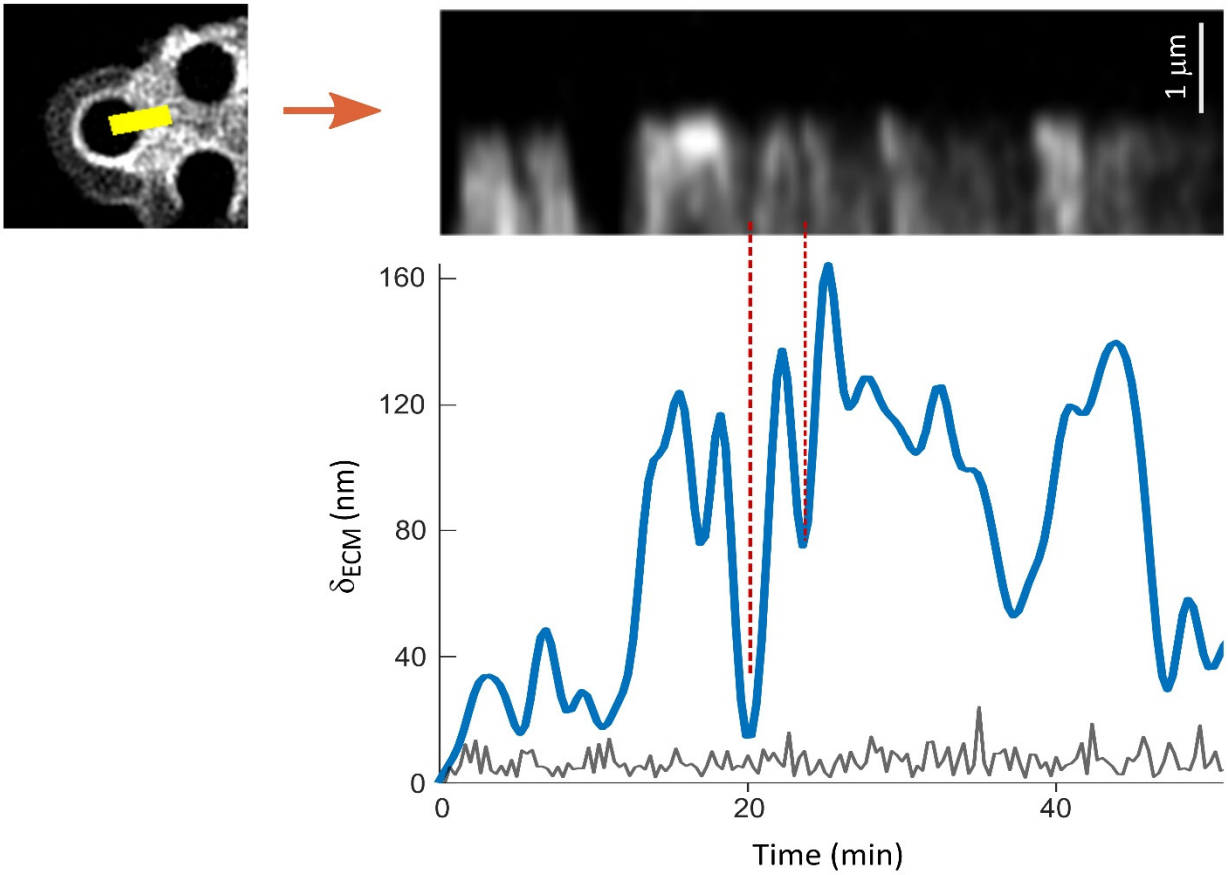

Supplementary Figure 4. Kymograph of tractin intensity taken from the edge of a single pillar (yellow rectangle in the left image was used to generate the kymograph) aligned with the displacement graph of the same pillar. Note the example of a single period between the dotted lines with simultaneous rise and drop in tractin intensity and in δ_{ECM}. Grey curve is the displacement noise (pillar that was not in contact with the cell throughout the experiment).

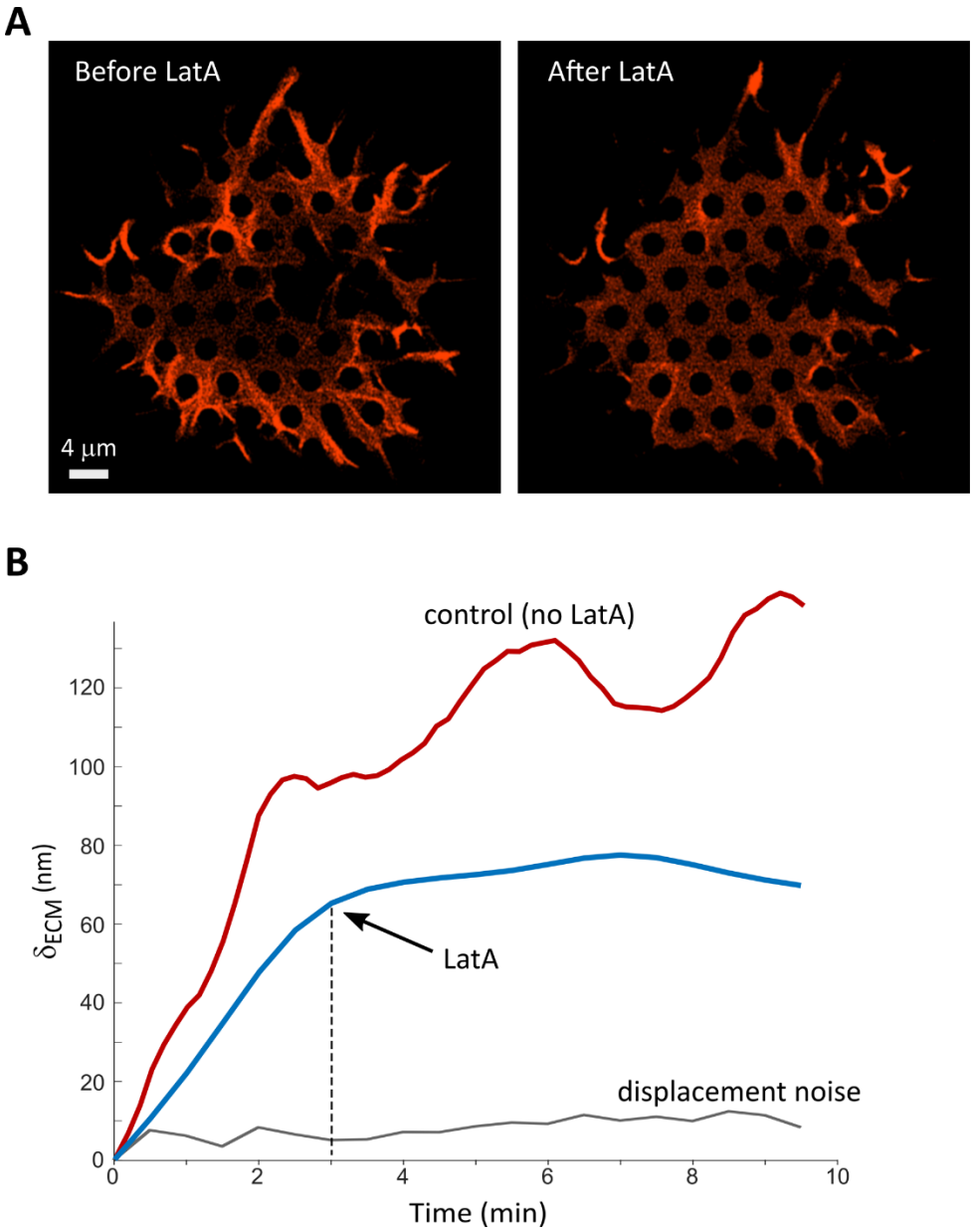

Supplementary Figure 5. Latrunculin A treatment blocks pillar displacement. (A) Images from a video of a MEF spreading on 2µm diameter pillars (stiffness = 31pN/nm) immediately before and immediately after addition of 330nM Latranculin A (LatA). Time difference between the two images is 30 s. (B) Example of a displacement curve of a single pillar (blue) whose movement was immediately blocked by LatA addition. Grey curve is the displacement noise (pillar that was not in contact with the cell throughout the experiment). Red curve is an example of pillar displacement by a cell that was not treated with LatA.

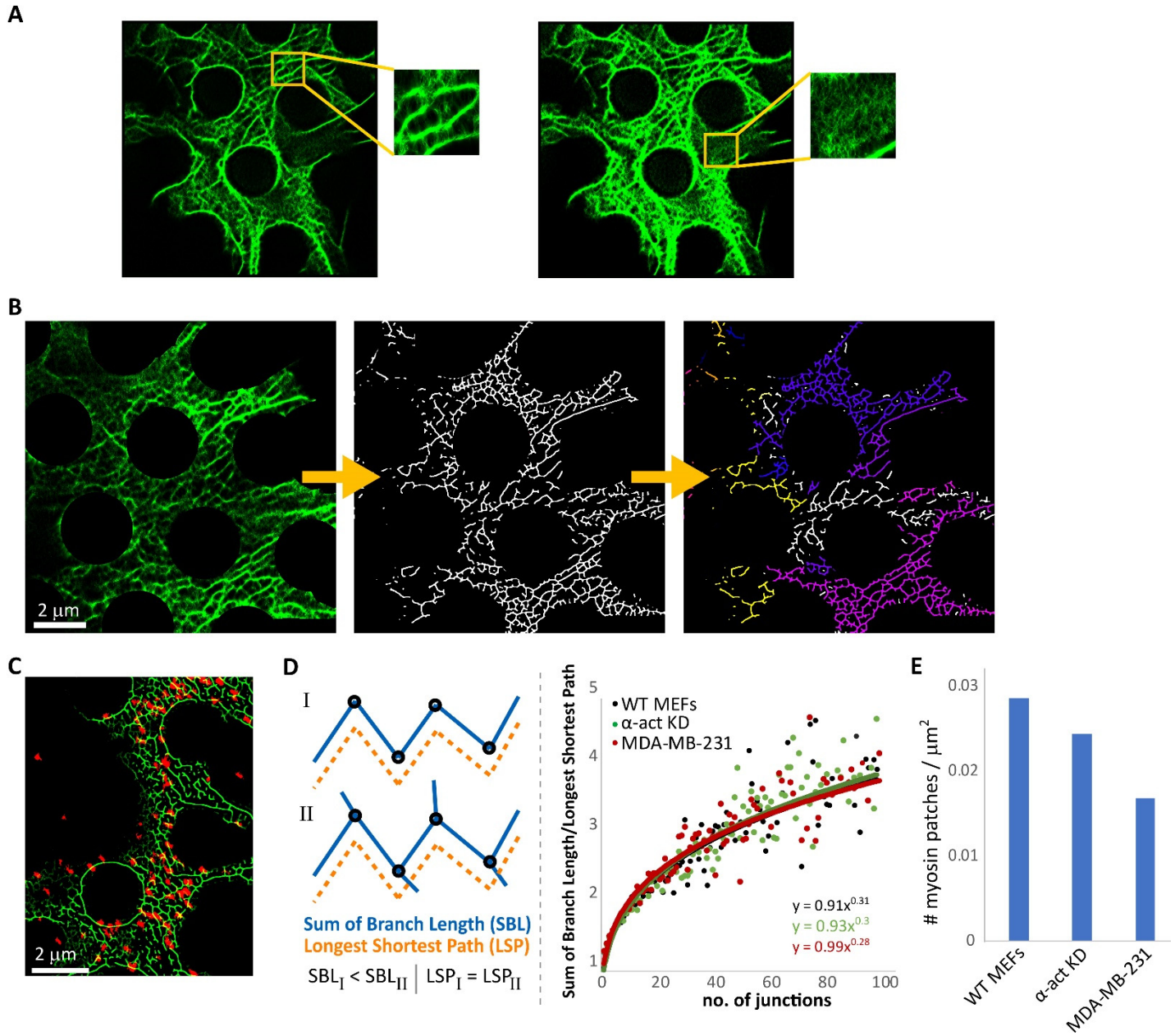

Supplementary Figure 6. Characterization of F-actin and p-myosin organization. (A) Images of a section of the cell edge on 2µm pillars stained for F-actin (bottom-left corner of the image is outside of the cell). The same image is presented twice, with decreased and enhanced brightness (left and right, respectively). The left zoom-in shows micron-scale actin structures whereas the right zoom-in shows nanometer-scale unstructured filaments. Box size in both cases is 1.7µm x 1.7µm. (B) Example of a super-resolution image of F-actin used to characterize the organization of the micron-scale actin structures between the pillars (top and right sides of the image are outside of the cell). Left: original image. Middle: segmented image. Right: analysis of the segmented image for continuous skeletons; each hue represents a single coherent skeleton. (C) Overlay of p-myosin (red) and F-actin (green) at the cell edge (right side of the image is outside of the cell). (D) Analysis of skeletons' complexity. We defined complexity as the ratio between the sum of branch length and the longest shortest path of each skeleton. In the example given on the left, both skeletons have the same shortest longest path; however, skeleton II, which is more complex, has a higher sum of branch length. Right: ratio of sum of branch length and the longest shortest path as a function of the number of junctions. No difference is observed between the three cell lines. For clarity purposes, each data point presented here is the average ratio for each no. of junctions (n>1500 skeleton all together, from >33 cells in each case, out of which >300 skeletons had 10 or more junctions). (E) Mean number of myosin clusters per μm^2 for each cell line.

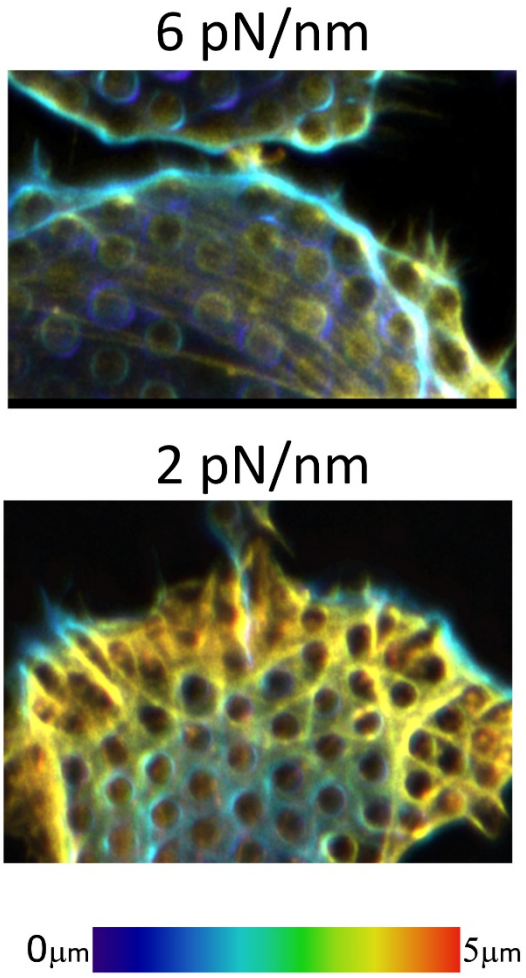

Supplementary Figure 7. Z-stack projections of the edges of REF52 cells on 2 and 6pN/nm pillars stained for F-actin color-coded for depth after 5h of spreading. F-actin around the pillars at the edge (blue hues) are connected to stress fibers 2-4μm above (yellow hues). Thick actin stress fibers (yellow-orange hues) are observed 2-4μm above the fibers directly surrounding the pillar (blue hues).

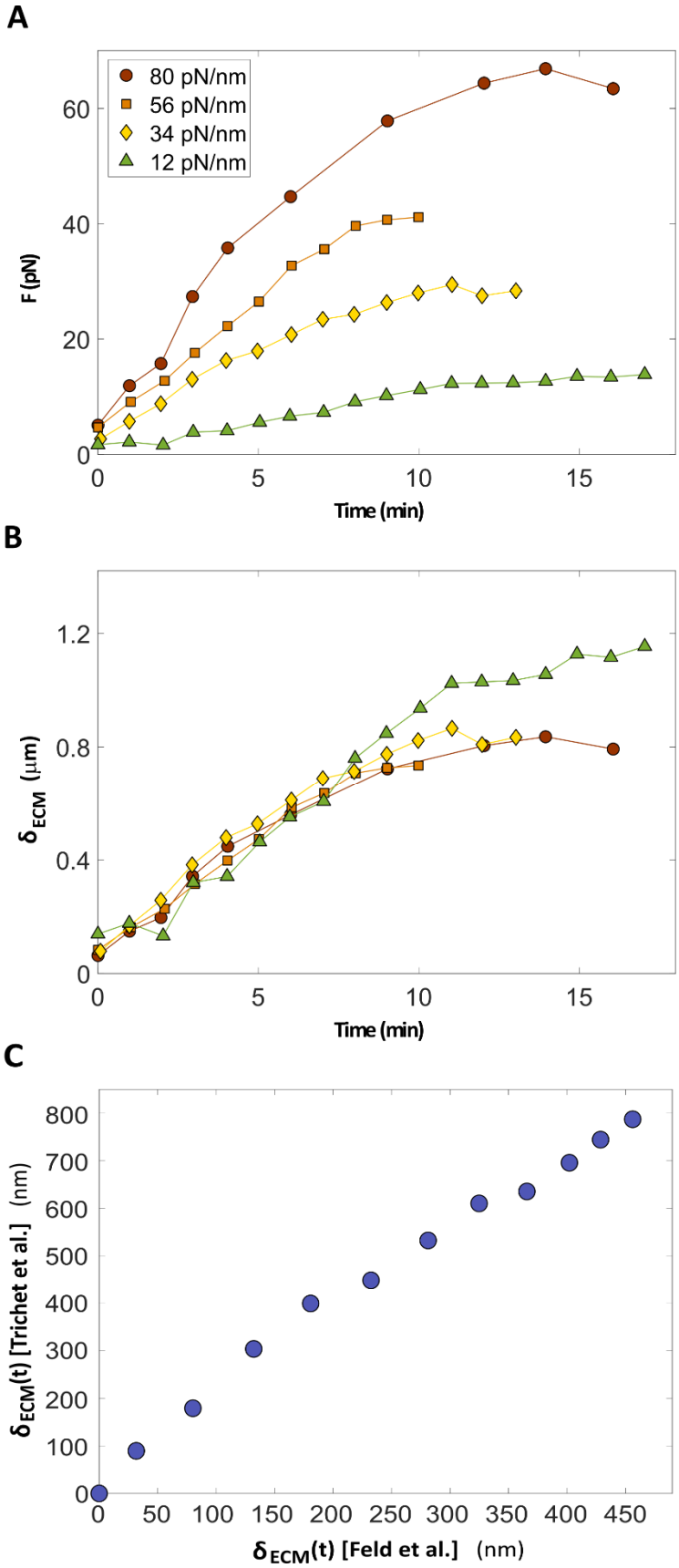

Supplementary Figure 8. (A) $F(t, k_{ECM})$ curves with different k_{ECM} values were extracted from Fig. 2A of Trichet et al. Note that in the original publication data for k_{ECM} = 4.7 pN/nm are also presented; however, the size of the symbols there is comparable to the actual measurement values, preventing reliable extraction of these data. (B) Replotting of the data in panel A in the rescaled form, $F(t, k_{ECM})/k_{ECM}$. (C) $\delta_{ECM}(t) = F(t, k_{ECM})/k_{ECM}$ of REF52 cells under well-spread steady-state conditions as measured in this work (Fig. 5B) vs. that measured by Trichet et al. (panel B here).